Soft Matter

PAPER

View Article Online
View Journal | View Issue

Cite this: *Soft Matter*, 2015, **11**, 1991

Structural studies of the lamellar to bicontinuous gyroid cubic (Q_{II}^{G}) phase transitions under limited hydration conditions†

T.-Y. Dora Tang,*[a] Nicholas J. Brooks,[b] Oscar Ces,[b] John M. Seddon[b] and Richard H. Templer[b]

Received 8th December 2014
Accepted 14th January 2015

DOI: 10.1039/c4sm02724h

www.rsc.org/softmatter

Non-equilibrium pathways of lyotropic phase transitions such as the lamellar to inverse bicontinuous cubic phase transition are important dynamical processes resembling cellular fusion and fission processes which can be exploited in biotechnological processes such as drug delivery. However, utilising and optimising these structural transformations for applications require a detailed understanding of the energetic pathways which drive the phase transition. We have used the high pressure X-ray diffraction technique to probe the lamellar to Q_{II}^{G} phase transition in limited hydration monolinolein on the millisecond time scale. Our results show that the phase transition goes *via* a structural intermediate and once the Q_{II}^{G} phase initially forms the elastic energy in the bilayer drives this structure to its equilibrium lattice parameter.

Introduction

Under certain conditions, mixtures of amphiphiles and water will form lyotropic liquid crystalline phases, with different degrees of hierarchical organisation. Examples of which include the lamellar phase (1-d), hexagonal phase (2-d) and the bicontinuous or micellar cubic phases (3-d). The inverse bicontinuous cubic phases have attracted attention for applications in drug delivery,[1–3] renewable energies[4–6] and protein crystallography[7–10] due to their large surface area to volume ratio, high water content and controllable and tuneable structural properties. Interestingly, it has been recognised, that these nanostructures resemble biological membrane architectures present in the cell membrane of eukaryotic cells, mitochondria, chloroplasts and the endoplasmic reticulum and that they are significant in dynamic biological processes such as membrane fusion and fission.

The formation of these curved mesophases, from amphiphilic molecules such as surfactants, polymers and lipids is driven by the hydrophobic effect,[11] head–group head–group interactions, curvature elastic stress and packing energy[12] and other small contributions such as electrostatic interactions. Within an amphiphilic bilayer there is an intrinsic desire for the monolayer leaflets to curve due to differences in the lateral pressure along the amphiphile length and this is known as the curvature elastic stress (CES). The CES within the bilayer can be relieved if the monolayer curves, however, this can result in a large energetic cost associated with the formation of hydrophobic voids within the bilayer. This energetic cost may be minimised by deforming the hydrocarbon chains, within the bilayer, from their preferred conformation to fill the hydrophobic voids (packing energy). The balance of curvature elastic stress and packing energy leads to an energy minimum which, under suitable circumstances favour the stable formation of the inverse bicontinuous phases. The resulting structure consists of a curved bilayer which subdivides three dimensional space into two non-penetrating but intertwined water channel networks, where the bilayer midplane lies upon a triply periodic minimal surface of zero mean curvature. The inverse bicontinuous cubic phases differ in the connectivity of the water channels, for example, in the Q_{II}^{G} phase the water channels are connected 3-fold at 120°, whilst the junctions in the Q_{II}^{D} phase connect 4-fold at 109° and 6-fold at 90° in the Q_{II}^{P} phase.

The energetics of the curved bilayers that make up the Q_{II} phases can be modelled from the pivotal surface; a surface through each monolayer where the area remains constant on isothermal bending. The pivotal surface can be described by either the parallel interface model (PIM)[13] or the constant mean curvature model (CMCM).[14,15] In the PIM, the pivotal surface lies equidistant and normal from the bilayer midplane whereas in the CMCM, the interface adopts a constant mean curvature meaning that the distance between the bilayer midplane and the pivotal surface must vary. While the PIM and CMCM define different geometries for the pivotal surface, recent studies have shown that there is no difference, within experimental error,

[a]*School of Chemistry, University of Bristol, Cantock's Close, Bristol BS8 1TS, UK. E-mail: chtydt@bristol.ac.uk*

[b]*Department of Chemistry, Imperial College London, Exhibition Road, London, SW7 2AY, UK*

† Electronic supplementary information (ESI) available: further information about peak intensity calculation, list of pressure jumps performed and plots of the volume fractions of all components for each pressure jump. See DOI: 10.1039/c4sm02724h

between the pivotal surface parameters obtained from the PIM and CMCM. However, it is important to note that the difference between the models does become significant when modeling the curvature energy of the inverse bicontinuous phases.[16]

Theoretical models for dynamic membrane fusion processes have shown that membrane bending elasticity is an important factor in fusion processes[17,18] and it has been generally accepted that the stalk model is the most energetically viable route for lipid bilayers to fuse.[19–23] During this process, transient contacts between lipid membranes are formed which widen and break to form interlamellar attachments (ILAs) or fusion pores. These structures are believed to be intermediaries in membrane fusion and the precursors to the formation of the tubular connections that are required for the formation of the inverse bicontinuous cubic phases from the lamellar phase. Experimental evidence for the stalk model is limited, but X-ray studies probing the lamellar to Q_{II}^{D} phase transition in excess water monoolein have shown evidence for the presence of stalks during the phase transition.[24] In addition, regularly arranged ILA pores have been imaged using CRYO-TEM (Transmission Electron Microscopy) during the lamellar to Q_{II}^{D} phase transition of synthetic lipid systems stabilized with polymers.[25] Taking together this previous experimental work and theoretical modelling the lamellar to inverse bicontinuous phase transition appears to be a suitable model for investigating membrane fusion processes which occur *via* the stalk model and where ILAs are structural intermediates of the phase transition. The stability of the inverse bicontinuous cubic phases is dependent on the pressure, temperature and pH,[5,26–30] and so any of these variables can be used as a structural change trigger to study the kinetics of cubic phase transitions. Pressure changes have significant advantages over the other triggers as they can be applied extremely quickly (on the ms timescale), both up and down in pressure, and moderate pressure does not tend to cause changes in intra-molecular bonding.[31]

To date there have been no investigations of lamellar to non-lamellar phase transitions under limited hydration conditions due to experimental difficulties in reproducibility and sample preparation. However, studying lamellar to inverse bicontinuous cubic phase transitions under limited hydration conditions presents several advantages: it allows quantitative investigation of the movement of water during the phase transitions and changes in molecular shape parameters of the lipid such as $\langle A_n \rangle$, and the lipid length can be followed during the phase transitions by applying suitable geometric models. Issues with sample preparation and reproducibility in limited hydration lipid samples have been overcome and we have used pressure-jump time-resolved small angle X-ray diffraction to study the dynamics of the lamellar to Q_{II}^{G} phase transition in limited hydration monolinolein. Pressure, was exploited as a structure change trigger in these experiments as its fast propagation allows decoupling of the trigger from structural changes within the lipid system, which take place on the millisecond time scale.

Our results show consistent trends in the out-of-equilibrium phase behaviour, across 11 different pressure jumps of different amplitudes. The trends are also consistent with those observed in the lamellar to Q_{II}^{D} phase transition of monoolein in excess water conditions[24] indicating that the lamellar to Q_{II}^{G} phase transition in limited hydration monolinolein goes *via* a structural intermediate (involving uncorrelated ILAs). Further analysis of our X-ray data gives supporting evidence of a non-diffracting intermediate structure in the lamellar to Q_{II}^{G} phase transition. In addition, we have been able to obtain the water volume fraction, $\langle A_n \rangle$ and the length of the lipid within the Q_{II}^{G} phase as the structure grows over time. We show that the Q_{II}^{G} phase initially forms with a stretched bilayer and is highly swollen, and as the Q_{II}^{G} phase matures the stretched bilayer relaxes to relieve the elastic energy within the bilayer and drives the Q_{II}^{G} phase to its equilibrium lattice parameter.

Materials and methods

Sample preparation

Known masses of lyophilized monolinolein (ML) (Larodan, Switzerland) and HPLC grade water (Sigma Aldrich, UK) were mixed to make samples with 22 wt% water. The mass of the lipid and water was measured to a precision of 0.001 mg giving an estimated error of $\pm$0.2 wt% error in the composition. The lipid–water samples were homogenized by subjecting them to at least 50 freeze–thaw cycles (-70 °C to 20 °C) and then stored at -20 °C until use. For the pressure-jump SAXS measurements, the lipid–water mixtures were transferred to Teflon sample holders shaped like an O-ring with mylar windows which contained and isolated the sample from the pressurizing medium.

Pressure jump X-ray scattering

Pressure-jump time-resolved SAXS experiments were performed at the high brilliance SAXS beamline ID02, European Synchroton Radiation Facility (ESRF), Grenoble, France using a custom built high pressure cell[32] capable of withstanding hydrostatic pressures up to 4000 bar and applying pressure jumps anywhere in the range 1 to 3000 bar (300 MPa) in 5 ms.

The temperature of the pressure cell was measured *via* a thermocouple embedded into the body of the cell and controlled *via* a circulating water bath to achieve a temperature stability of 0.1 °C. The high pressure cell uses 1 mm thick type IIa diamond windows providing an X-ray transmission of approximately 65% at an X-ray of energy of 17 keV ($\lambda = 0.75$ Å). Samples were further homogenised after loading into the pressure cell by subjecting them to 10 pressure cycles from 1 bar to 2000 bar. To allow for equilibration, samples were incubated for at least 30 minutes after each change in temperature. Pressure jumps were designed according to the pressure–temperature phase diagrams determined previously[5] and the pressure jump amplitude was defined as the pressure difference between the lamellar to lamellar/Q_{II}^{G} coexistence phase boundary and the final pressure of the jump. After every pressure jump, the sample pressure was reduced to 1 bar, left to equilibrate for 2 min and then returned to the starting pressure. The pressure jump was triggered by a TTL pulse to the pressure valves on the acquisition of the 3rd image at time = 0 s. X-ray diffraction images were captured using a Frelon (Fast readout, low noise)

Kodak CCD detector with a maximum frame rate of 15 frames per s and with a typical exposure time of 0.1 s. The beamline software automatically corrects the data to absolute scattering intensities (number of scattered photos per sterrad per incident photon).

Data reduction

Diffraction images were analysed offline using custom built software developed using National Instruments LabVIEW. The lattice parameter was calibrated using silver behenate (a = 58.38 Å) giving a final estimated error in the determined lattice parameter of ±0.05 Å. Accurate diffracted intensities were obtained by subtracting a suitable and consistent background, which is important for accurate and reliable absolute intensity analysis. The background was obtained by excluding the diffraction peaks from a radially averaged 1D plot of the diffraction pattern, which was then fitted to a 4th order polynomial. The background was then subtracted from the diffraction pattern (see ESI† for further information). Instrumental data were applied transparently by the beam line software (Fig. SI1†) and so the absolute intensity of each diffraction peak was obtained by integrating the total intensity under each peak, and then normalising to the sample thickness. The absolute intensity of the (100) peak for the lamellar phase and (211) peak for the Q_{II}^{G} phase were used to determine the volume fraction of each phase during the phase transitions.

Obtaining initial rates from kinetic data

The Avrami model[33–35] (eqn (1)) was used to fit the absolute intensity of the Q_{II}^{G} phase as a function of time to obtain the rate constant, k, for each of the 11 pressure jumps.

$$I_t = I_{max}(1 - e^{-(kt)^n}) \quad (1)$$

I_t is the integrated absolute intensity at time, t of the 1st diffraction peak of the mesophase. I_{max} is the maximum absolute intensity and n is the dimensionality of domain growth (n was fit as a free fitting parameter).

Determination of the volume fraction of the intermediate phase

The intermediate phase during the lamellar to Q_{II}^{G} transition was obtained by analysis of the total intensity at a given time which is normalised to the starting intensity of the lamellar phase, 1, at t = 0 s, and to the end intensity of the lamellar phase, 0, at $t = \infty$ assuming that the phase transition has gone to completion. According to diffraction conditions and assuming that every part of the sample will diffract when it is either in the lamellar or in the Q_{II}^{G} phase, the total intensity at a given time will be equal to 1. If some part of the sample does not diffract then the total intensity is ⟨1, and the volume fraction of the non-diffracting intermediate, can be calculated from the total intensity at time, t, using eqn (2).

$$\phi_{intermediate} = 1 - \phi_{total} = 1 - \left(\phi_{lam} + \phi_{Q_{II}^{G}}\right) \quad (2)$$

where $\phi_{lam} = \left(\frac{I_t}{I_{t=0}}\right)_{lam}$ and $\phi_{Q_{II}^{G}} = \left(\frac{I_t}{I_{t=\infty}}\right)_{Q_{II}^{G}}$ for a lamellar to Q_{II}^{G} phase transition.

Obtaining lipid length and $\langle A_n \rangle$

The parallel interface model for the Q_{II}^{G} phase is defined by eqn (3) and relates the measured lattice parameter, a, to the water volume fraction, ϕ_w. Where $\langle v \rangle$ is the molecular volume and is a measured parameter, σ is the dimensionless surface area (3.0915 for Q_{II}^{G}),[36–38] and χ is the Euler characteristic (−8 for Q_{II}^{G}). $\langle A_n \rangle$ is the area at the pivotal surface, $\langle v_n \rangle$ is the volume between the bilayer midplane and the pivotal surface and are variables which can be determined by applying a non-linear fit using Mathematica (Wolfram, Hanborough, UK).

During the pressure jump $\langle v_n \rangle$, $\langle A_n \rangle$ and $\langle v \rangle$ are assumed to be constant and take their values from the pressure and temperature at the end of the jump, inputting these values and the experimental lattice parameter into eqn (3) allows one to solve for ϕ_w and determine ϕ_l.

The change in lipid length, l, and $\langle A_n \rangle$ during the phase transition can be calculated using eqn (4) and (5) respectively. Eqn (4) relates l to the lipid volume, ϕ_l, and eqn (5) relates $\langle A_n \rangle$

$$a = \frac{\langle v \rangle}{\langle A_n \rangle (1 - \phi_w)} \left\{ -2\sigma + \frac{2^{\frac{5}{3}}\,\sigma^2}{\sqrt[3]{4\sigma_0{}^3 + 9\pi\chi\,(1 - \phi_w)^2 \left(\frac{\langle v_n \rangle}{\langle v \rangle}\right)^2 + 3(1 - \phi_w)\left(\frac{\langle v_n \rangle}{\langle v \rangle}\right)\sqrt{\pi\chi\left(8\sigma_0{}^3 + 9\pi\chi\,(1 - \phi_w)^2 \left(\frac{\langle v_n \rangle}{\langle v \rangle}\right)^2\right)}}} \right.$$
$$\left. + \frac{2^{\frac{1}{3}}}{\sqrt[3]{4\sigma_0{}^3 + 9\pi\chi\,(1 - \phi_w)^2 \left(\frac{\langle v_n \rangle}{\langle v \rangle}\right)^2 + 3(1 - \phi_w)\left(\frac{\langle v_n \rangle}{\langle v \rangle}\right)\sqrt{\pi\chi\left(8\sigma_0{}^3 + 9\pi\chi\,(1 - \phi_w)^2 \left(\frac{\langle v_n \rangle}{\langle v \rangle}\right)^2\right)}}} \right\} \quad (3)$$

to the distance, ξ, from the bilayer midplane to the pivotal surface. ξ can be obtained from eqn (7). $\langle K \rangle$ is the surface averaged Gaussian curvature at the bilayer interface.

$$\phi_l = 2\,\sigma\left(\frac{l}{a}\right) + \frac{4}{3}\pi\chi\left(\frac{l}{a}\right)^3 \quad (4)$$

$$\langle A_n \rangle = \frac{\langle v_n \rangle}{\xi}\left(\frac{1+\langle K\rangle\xi^2}{1+\frac{1}{3}\langle K\rangle\xi^2}\right) \quad (5)$$

$$\langle K \rangle = \frac{2\pi\chi}{\sigma a^2} \quad (6)$$

$$\left(\frac{\langle V_n \rangle}{\langle V \rangle}\right)\phi_l = 2\,\sigma\left(\frac{\xi}{a}\right) + \frac{4}{3}\pi\chi\left(\frac{\xi}{a}\right)^3 \quad (7)$$

Results

The pressure-jump time resolved X-ray diffraction technique was employed to investigate the mechanism of the lamellar to Q_{II}^G phase transition in limited hydration monolinolein (22 wt%) (Fig. 1). Analysis of 11 pressure jumps, from high pressure to low pressure, across a range of pressure jump amplitudes showed consistent trends in the lattice parameter evolution and absolute intensities for the lamellar and Q_{II}^G phase. In addition our results show evidence for a non-diffracting intermediate (assumed to be ILAs) giving experimental support for the stalk mechanism in the lamellar to inverse Q_{II}^G phase transition.

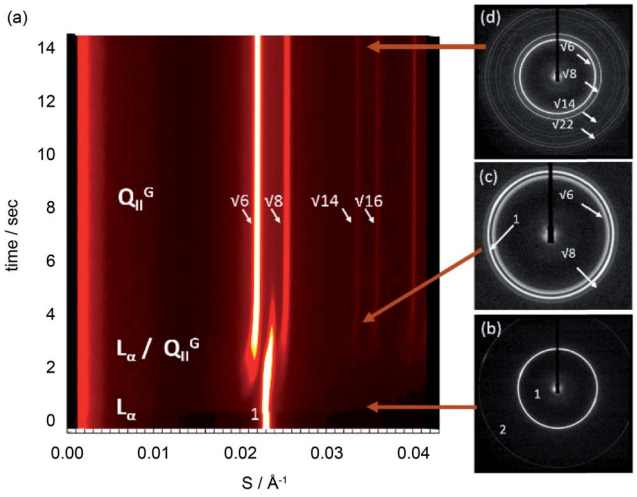

Fig. 1 (a) Stacked diffraction plot showing the diffraction pattern during a lamellar to Q_{II}^G transition triggered by a pressure jump from $P_{start} = 1800$ bar to $P_{end} = 440$ bar with $P_{amp} = -835$ bar (where P_{amp} is defined as the pressure difference between the lamellar–lamellar/Q_{II}^G phase boundary and the end of the pressure jump (P_{end})). Typical 2D diffraction patterns from (b) the lamellar phase before the start of the jump, (c) lamellar and Q_{II}^G phase coexistence during the pressure jump (enlarged for clarity) and (d) and the Q_{II}^G phase at the end of the pressure jump.

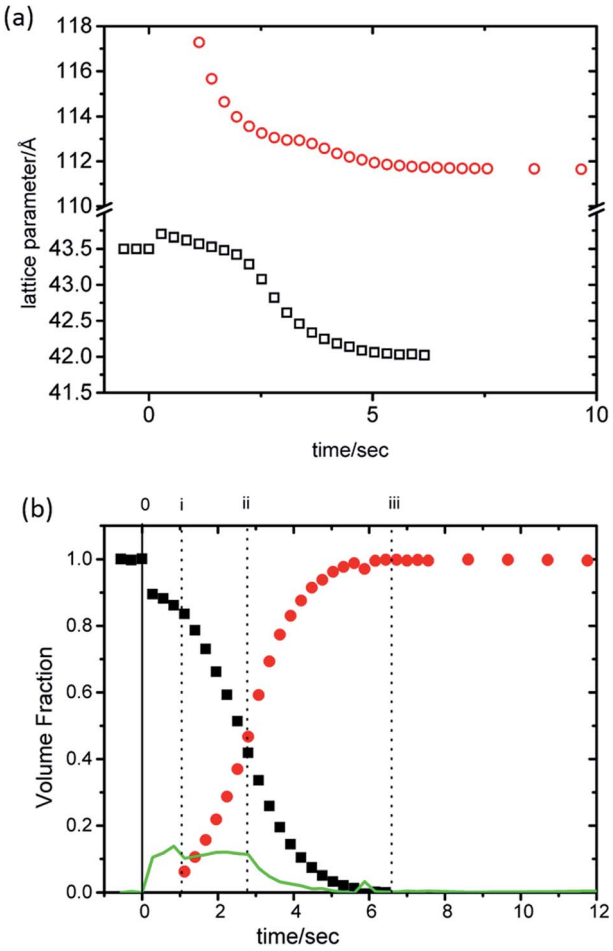

Fig. 2 Structural changes of the lamellar and Q_{II}^G phase during a pressure jump ($P_{start} = 1800$ bar, $P_{end} = 440$ bar, $P_{amp} = -835$ bar) starting in the lamellar phase, time = 0 denotes time of pressure jump. (a) Changes in the lattice parameter of the outgoing lamellar phase (black open squares) and the incoming Q_{II}^G phase (red open circles); (b) changes in the volume fraction of the lamellar phase (black closed squares), Q_{II}^G phase (red closed circles) and the non-diffracting structural intermediate (green line).

Immediately after the pressure jump ($t = 0$ s), there is an increase in the lamellar lattice parameter of approximately 0.2 Å (Fig. 2a). Equilibrium studies have shown that a decrease in hydrostatic pressure leads to a decrease in the lamellar lattice parameter,[5] therefore the increase in layer spacing immediately after the pressure jump is not a direct effect of pressure on the lamellar phase. We attribute the 0.2 Å increase in the lamellar lattice parameter and the accompanying decrease in the absolute intensity to the formation of non-diffracting structural intermediates which we assume to be ILAs (however it should be noted that the decrease in intensity could also arise from the formation of other non-diffraction intermediates). As a consequence of lipid rearrangement within the bilayer there is local displacement of water around the ILA 'defects' causing an increase in spacing between the bilayers. We believe that the subsequent decrease in the absolute intensity of the lamellar phase is due to an increase in the number of bilayer lipids

which make up the non-correlated (and so non-diffracting) ILA structures which do not contribute to the diffracted intensity.

Analysis of the diffraction intensity to obtain the volume fraction of the lamellar and Q_{II}^{G} phases (see Materials and methods) allowed us to quantify the relative percentage of the non-diffracting intermediate during the time-course of the pressure jump. Our results show that immediately after the pressure jump (Fig. 2b, $t = 0$ and Fig. S2†) there is an increase in the volume fraction of the ILAs until a critical fraction of the sample is non-diffracting (typically between 5 and 35% of the total volume fraction).

The critical amount is dependent on the formation, diffusion and arrangement of the ILAs prior to the formation of the Q_{II}^{G} phase where the ILAs adopt a specific configuration, most likely based on an energy minimum prior to the formation of the Q_{II}^{G} phase. Once this takes place, the volume fraction of ILA decreases as they transform into the water channels of the Q_{II}^{G} phase. The packing of ILAs prior to Q_{II}^{G} formation is still unclear but it is interesting to note that the Q_{II}^{G} phase begins to appear when as little as 5% of the volume fraction of the lamellar phase forms non-diffracting intermediates suggesting that the formation of the Q_{II}^{G} phase is dependent on the local number and configuration of the ILAs. Our results also show that the initial formation and the rate of equilibration of the Q_{II}^{G} phase is dependent on the pressure jump amplitude, *i.e.* increasing the pressure jump amplitude leads to faster appearance and equilibration of the Q_{II}^{G} phase (as expected based on previous studies[39]). This suggests that the random formation and diffusion prior to Q_{II}^{G} phase formation could be dependent on the pressure jump amplitude (Fig. 3 and S2†). In addition, we observe a decrease in the dimensionality constant, n, as the pressure jump increases (Fig. 3b) from 2.49 $\pm$ 0.04 ($P_{amp} = -965$ bar) to 2.81 $\pm$ 0.10 ($P_{amp} = -685$ bar). A non-integer value, for n between 2 and 3 indicates that nucleation sites form at the beginning of the reaction and as the transition progresses.

Once the Q_{II}^{G} phase forms, the volume fraction of the intermediate phase remains fairly constant suggesting that the rate of ILA formation is equal to the rate of Q_{II}^{G} phase formation. Once the lamellar phase decreases to approximately half its initial amount, the ILA concentration begins to decrease and approaches zero, whilst the rate of Q_{II}^{G} phase formation increases. Therefore, once the Q_{II}^{G} phase forms, the rate of cubic phase formation is no longer dependent on the formation and diffusion of ILAs suggesting that the rate determining step for Q_{II}^{G} formation is the alignment of ILAs into the correct energy configuration prior to tubule formation.

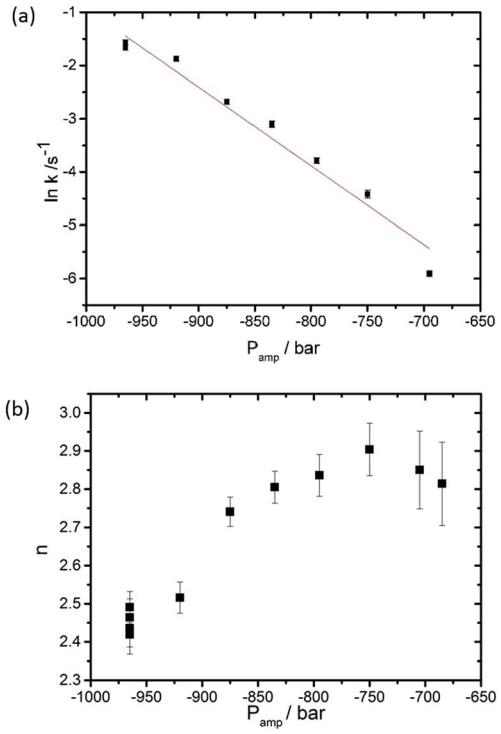

Fig. 3 Effect of the pressure jump amplitude (a) on the rate of Q_{II}^{G} phase growth and (b) on n, the dimensionality constant, based on 11 pressure-jump measurements carried out at 26 °C.

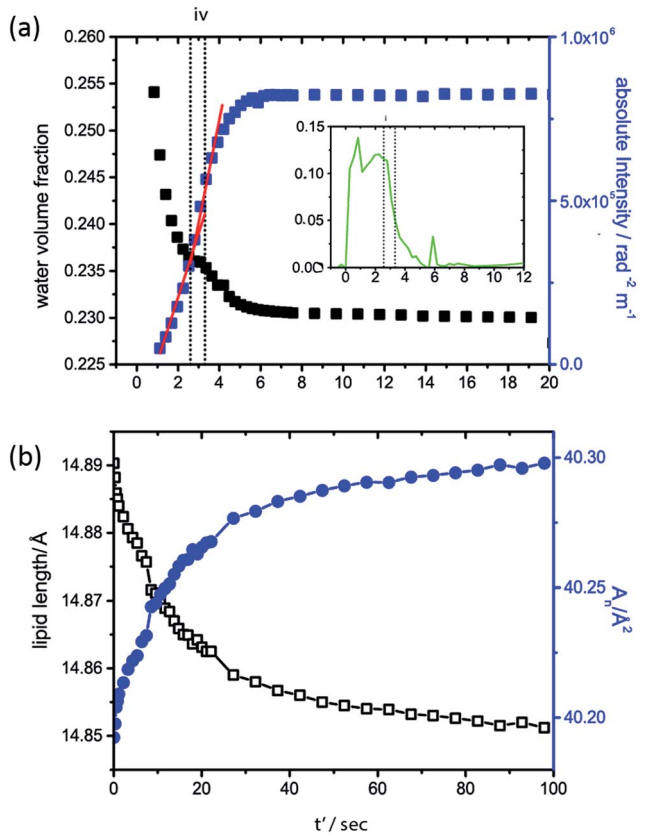

Fig. 4 Structural changes of the Q_{II}^{G} phase after initial formation (note that t′ is the time after initial formation of the Q_{II}^{G} phase). (a) Changes to the water volume fraction (black closed squares) of the Q_{II}^{G} phase after formation and the changes in the absolute intensity (blue closed squares) of the Q_{II}^{G} diffraction pattern; vertical dashed lines marked (iv) indicate constant water content of the Q_{II}^{G} phase. Inset shows the change in volume fraction of the non-diffracting structural intermediate. (b) Changes to the lipid length (black open squares) and $\langle A_n \rangle$ (blue closed squares) as the Q_{II}^{G} matures after initial formation (designated $t' = 0$).

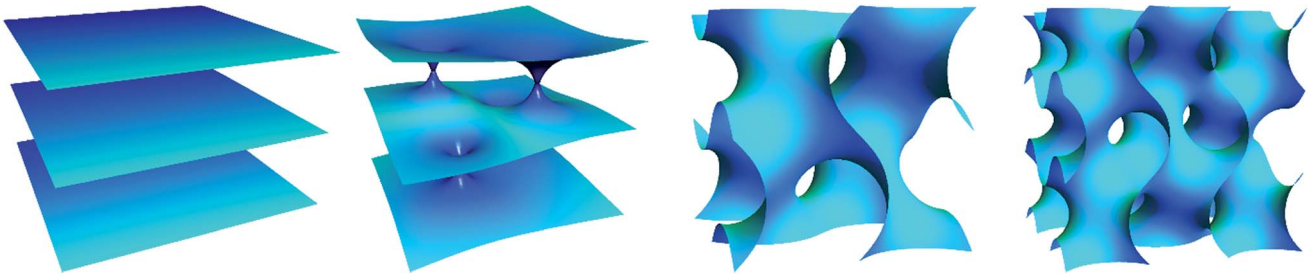

Fig. 5 Summary of the proposed transition from a flat lamellar structure to an inverse bicontinuous cubic gyroid phase. The figures show the bilayer mid-plane in (from left to right): flat lamellar phase, uncorrelated inter-lamellar attachments (ILAs), swollen gyroid structure, equilibrium gyroid phase.

To further investigate the driving force for Q_{II}^{G} maturation after initial Q_{II}^{G} formation, the water volume fraction of the Q_{II}^{G} phase and the absolute intensity of the (100) and (211) diffraction peaks of the lamellar and Q_{II}^{G} phase respectively were determined (Fig. 4a) as a function of time, assuming that $\langle v \rangle$, $\langle v_n \rangle$ and $\langle A_n \rangle$ are constant throughout the maturation period. Our analysis shows that the Q_{II}^{G} phase is initially swollen, formed with a large water volume fraction, consistent with a stretched bilayer, low interfacial curvature and a large pore size (Fig. 5).

After initial formation of the Q_{II}^{G} phase there is subsequent increase in the absolute intensity of the inverse bicontinuous cubic phase and a concomitant decrease in the water volume fraction. This indicates that the Q_{II}^{G} phase initially forms with a small number of unit cells with high water content and as the number of unit cells and water channels of the cubic phase increase *i.e.* as the Q_{II}^{G} phase matures the water content of the unit cell decreases. A plateau in the water volume fraction in the Q_{II}^{G} phase is observed, less than a second after the first appearance of the Q_{II}^{G} phase (Fig. 4 iv), which coincides with a decrease in volume fraction of the intermediate phase. This is observed consistently throughout the 11 pressure jumps (Fig. S2†). This suggests that the formation of a swollen cubic phase is promoted by an increased local water concentration made available by the formation of ILAs. These results are consistent with a period of maximum growth rate of the Q_{II}^{G} structure (indicated by the red line, Fig. 4) where the desire to increase the number of unit cells and water channels is driven by a desire to reduce the elastic energy of the bilayer which is initially stretched.

Determination of the change in lipid length and the area per lipid at the pivotal surface once all the lamellar phase and intermediate has disappeared at iii (Fig. 2b) (designated $t' = 0$ in Fig. 4b for clarity) show that as the Q_{II}^{G} phase matures, the lipid length decreases and the area at the pivotal surface increases. This signifies a change in the lipid shape from cylindrical-like to cone-like. Structural changes within the lipid alleviates the energetic cost of a stretched bilayer by increasing the negative interfacial curvature and relaxation from a stretched bilayer can be achieved by the growth of more unit cells with smaller pore size.

Conclusions

The pressure jump time-resolved X-ray diffraction technique was used to probe the lamellar to Q_{II}^{G} phase transition in limited hydration monolinolein. Analysis of 11 pressure jumps showed consistent qualitative trends and evidence of a non-diffracting intermediate which could be consistent with the ILAs described in the stalk model for lamellar to non-lamellar phase transitions. In addition, our results show that the initial Q_{II}^{G} phase is swollen with a stretched bilayer. The energetic drive to reduce the elastic energy in the stretched bilayer leads to the maturation of a Q_{II}^{G} phase towards thermodynamic equilibrium with increased number of unit cells and decreased water content.

Acknowledgements

This work was supported by EPSRC Platform Grant EP/G00465X/1, EPSRC Programme Grant EP/J017566 and by an EPSRC DTA studentship awarded to T-YDT. We acknowledge Diamond Light Source (UK) and the European Synchrotron Radiation Facility (Grenoble, France) for the provision of synchrotron radiation facilities and we would like to thank Dr Nick Terrill, Dr Claire Pizzey (beamline I22, DLS) and Dr Michael Sztucki (beamline ID02, ESRF) for their assistance during the synchrotron experiments. We thank Prof. Roland Winter and Dr Christoph Jeworrek at the University of Dortmund for the loan of their high pressure cell.

Notes and references

1 B. J. Boyd, D. V. Whittaker, S.-M. Khoo and G. Davey, *Int. J. Pharm.*, 2006, **309**, 218–226.
2 J. Bender, M. B. Ericson, N. Merclin, V. Iani, A. Rosen, S. Engstrom and J. Moan, *J. Controlled Release*, 2005, **106**, 350–360.
3 C. V. Kulkarni, T.-Y. Tang, A. M. Seddon, J. M. Seddon, O. Ces and R. H. Templer, *Soft Matter*, 2010, **6**, 3191–3194.
4 G. O. Hustad, T. Richardson, W. C. Winder and M. P. Dean, *Chem. Phys. Lipids*, 1971, **7**, 61–74.
5 T. Y. D. Tang, N. J. Brooks, C. Jeworrek, O. Ces, N. J. Terrill, R. Winter, R. H. Templer and J. M. Seddon, *Langmuir*, 2012, **28**, 13018–13024.
6 N. J. Brooks, B. L. L. E. Gauthe, N. J. Terrill, S. E. Rogers, R. H. Templer, O. Ces and J. M. Seddon, *Rev. Sci. Instrum.*, 2010, **81**, 064103.
7 V. Cherezov, *J. Mol. Biol.*, 2006, **357**, 1605–1618.

8 P. Nollert, H. Qiu, M. Caffrey, J. P. Rosenbusch and E. Landau, *Fed. Eur. Biochem. Soc., Lett.*, 2001, 179–186.
9 G. Rummel, A. Hardmeyer, C. Widmer, M. Chiu, P. Nollert, K. Locher, I. Pedruzzi, E. Landau and J. Rosenbusch, *J. Struct. Biol.*, 1998, 182–191.
10 G. Cevc, A. Watts and D. Marsh, *Biochemistry*, 1981, **20**, 4955–4965.
11 D. F. Evans and H. Wennerstrom, *The colloidal domain, where Physics, chemistry, biology and technology meet*, 1999.
12 G. L. Kirk, S. M. Gruner and D. L. Stein, *Biochemistry*, 1984, **23**, 1093–1102.
13 S. T. Hyde, *J. Phys. Chem.*, 1989, **93**, 1458–1464.
14 D. M. Anderson, S. M. Gruner and S. Leibler, *Proc. Natl. Acad. Sci. U. S. A.*, 1988, **85**, 5364–5368.
15 K. Grosse-Brauckmann, *J. Colloid Interface Sci.*, 1997, **187**, 418–428.
16 T.-Y. D. Tang, A. M. Seddon, C. Jeworrek, R. Winter, O. Ces, J. M. Seddon and R. H. Templer, *Soft Matter*, 2014, **10**, 3009–3015.
17 W. Helfrich and H. Rennschuh, *J. Phys. Colloq.*, 1990, **51**, C7-189–C7-195.
18 A. Efrat, L. V. Chernomordik and M. M. Kozlov, *Biophys. J.*, 2007, **92**, L61–L63.
19 Y. Kozlovsky, L. V. Chernomordik and M. M. Kozlov, *Biophys. J.*, 2002, **83**, 2634–2651.
20 Y. Kozlovsky and M. M. Kozlov, *Biophys. J.*, 2003, **85**, 85–96.
21 V. S. Markin, M. M. Kozlov and V. L. Borovjagin, *Gen. Physiol. Biophys.*, 1984, **3**, 361–377.
22 D. P. Siegel, *Biophys. J.*, 1999, **76**, 291–313.
23 Y. Kozlovsky, A. Efrat, D. A. Siegel and M. M. Kozlov, *Biophys. J.*, 2004, **87**, 2508–2521.
24 C. E. Conn, O. Ces, X. Mulet, S. Finet, R. Winter, J. M. Seddon and R. H. Templer, *Phys. Rev. Lett.*, 2006, **96**, 108102.
25 X. Mulet, X. Gong, L. J. Waddington and C. J. Drummond, *ACS Nano*, 2009, **3**, 2789–2797.
26 R. Winter and W. Dzwolak, *Philos. Trans. R. Soc., A*, 2005, **363**, 537–563.
27 A. Yaghmur, M. Kriechbaum, H. Amenitsch, M. Steinhart, P. Laggner and M. Rappolt, *Langmuir*, 2009, **26**, 1177–1185.
28 M. M. Alam, T. Oka, N. Ohta and M. Yamazaki, *J. Chem. Phys.*, 2011, **134**, 145102.
29 J. Barauskas and T. Landh, *Langmuir*, 2003, **19**, 9562–9565.
30 A. Chanturiya, L. V. Chernomordik and J. Zimmerberg, *Proc. Natl. Acad. Sci. U. S. A.*, 1997, **94**, 14423–14428.
31 R. Winter and R. Kohling, *J. Phys.: Condens. Matter*, 2004, **16**, S327–S352.
32 J. Woenckhaus, *Rev. Sci. Instrum.*, 2000, **71**, 3895–3899.
33 A. Melvin, *J Chem Phys*, 1939, **7**, 1103–1112.
34 A. Melvin, *J Chem Phys*, 1941, **9**, 177–184.
35 A. Melvin, *J Chem Phys*, 1940, **8**, 212–224.
36 S. T. Hyde, *J. Phys., Colloq.*, 1990, **51**, C7.
37 A. H. Schoen, *Report D-5541*, NASA, Washington DC, 1970.
38 A. Mackay and J. Klinowski, *Comput. Math. Appl.*, 1986, **12**, 803–824.
39 C. E. Conn, O. Ces, A. M. Squires, X. Mulet, R. Winter, S. Finet, R. H. Templer and J. M. Seddon, *Langmuir*, 2008, **24**, 2331.